PCCP

View Online
Dynamic Article Links

Cite this: DOI: 10.1039/c0cp01541e

www.rsc.org/pccp

PAPER

# A shock tube and theoretical study on the pyrolysis of 1,4-dioxane†

X. Yang,[a] A. W. Jasper,[b] B. R. Giri,‡[a] J. H. Kiefer[c] and R. S. Tranter*[a]

*Received 18th August 2010, Accepted 4th November 2010*
**DOI: 10.1039/c0cp01541e**



The dissociation of 1, 2 and 4% 1,4-dioxane dilute in krypton was studied in a shock tube using laser schlieren densitometry, LS, for 1550–2100 K with 56 ± 4 and 123 ± 3 Torr. Products were identified by time-of-flight mass spectrometry, TOF-MS. 1,4-dioxane was found to initially dissociate *via* C–O bond fission followed by nearly equal contributions from pathways involving 2,6 H-atom transfers to either the O or C atom at the scission site. The 'linear' species thus formed (ethylene glycol vinyl ether and 2-ethoxyacetaldehyde) then dissociate by central fission at rates too fast to resolve. The radicals produced in this fission break down further to generate H, $CH_3$ and OH, driving a chain decomposition and subsequent exothermic recombination. High-level *ab initio* calculations were used to develop a potential energy surface for the dissociation. These results were incorporated into an 83 reaction mechanism used to simulate the LS profiles with excellent agreement. Simulations of the TOF-MS experiments were also performed with good agreement for consumption of 1,4-dioxane. Rate coefficients for the overall initial dissociation yielded $k_{123\mathrm{Torr}} = (1.58 \pm 0.50) \times 10^{59} \times \mathrm{T}^{-13.63} \times \exp(-43970/\mathrm{T})\ \mathrm{s}^{-1}$ and $k_{58\mathrm{Torr}} = (3.16 \pm 1.10) \times 10^{79} \times \mathrm{T}^{-19.13} \times \exp(-51326/\mathrm{T})\ \mathrm{s}^{-1}$ for $1600 < T < 2100$ K.

## Introduction

Fuels derived from tar sands and oil shales contain a higher proportion of cyclic species than those derived from more conventional feedstocks and interest in the combustion mechanisms of these species is growing. One class of compounds that is of particular interest is the cyclic ethers which may be formed as intermediates in the combustion of non-traditional fuels. The literature concerning the kinetics and mechanisms of the pyrolysis and oxidation of cyclic ethers is sparse and we have accordingly decided to investigate the pyrolysis of some saturated cyclic ethers at high temperatures in the shock tube.

Cyclohexane (zero O-atoms) can be considered as the first of the series of saturated six-member rings that extends through pyran (one O-atom), 1,3- and 1,4-dioxane (two O-atoms) to 1,3,5-trioxane (three O-atoms). At the extremes of this series two distinct dissociation mechanisms are known to operate. 1,3,5-trioxane dissociates *via* a concerted mechanism to give three formaldehyde molecules[1–5] whereas shock tube studies of cyclohexane pyrolysis[6,7] demonstrated that cyclohexane dissociates *via* C–C fission followed by isomerization to 1-hexene and its dissociation.

The current work focuses on the dissociation of 1,4-dioxane previously studied at low temperatures by Kuchler and Lambert[8] and Battin *et al.*[9] Both these studies concluded that the dissociation involved a free radical mechanism. Battin *et al.* proposed the following: An initial scission of a C–C bond is followed by dissociation of the linear radical to formaldehyde and ethene, reaction (I), below. They suggested that homolysis of formaldehyde to H-atoms and formyl radicals would then initiate chain reaction through (II). However, at the temperatures and pressures of their study (33 Torr, 783 and 825 K) this cannot occur homogeneously in the gas phase because of the high thermal stability of formaldehyde[1,10,11] and also ethene.[12–15]

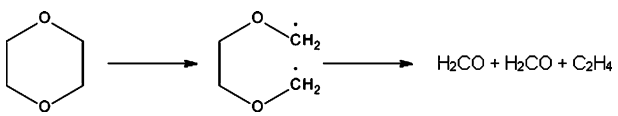


(I)

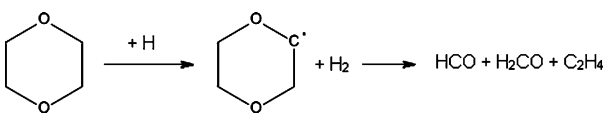


(II)

This early work is thus clearly wrong about the dissociation mechanism and the source of chain radicals. It is then appropriate that the dissociation and its products be reexamined.

[a] *Chemical Sciences and Engineering Division, Argonne National Laboratory, 9700 S. Cass Avenue, Argonne, IL-60439*
[b] *Combustion Research Facility, Sandia National Laboratories, P.O. Box 969, Livermore, CA-94551*
[c] *Department of Chemical Engineering, 810 S. Clinton St., University of Illinois at Chicago, Chicago, IL-60607*

† Electronic supplementary information (ESI) available: Table S1–S4. See DOI: 10.1039/c0cp01541e

‡ Current Address: Alberta Sulfur Research Ltd, 3535 Research Road NW, Calgary, Alberta T2L 2K8, Canada.

Given the high bond strengths expected in a molecule like 1,4-dioxane, examination of its dissociation will require high temperatures. The mechanism and kinetics of the pyrolysis of 1,4-dioxane have accordingly been investigated in the shock tube by laser schlieren densitometry, LS, and time-of-flight mass spectrometry, TOF-MS, experiments. These studies yield direct measures of both the initial rate of dissociation of 1,4-dioxane and the identities of products, which then guide development of a comprehensive mechanism for the pyrolysis. In addition to the experimental effort, the dissociation of 1,4-dioxane and its products has been investigated theoretically. As well as elucidating mechanistic details attempts were made to estimate several key rate coefficients by master equation analyses to provide initial estimates for the modeling work.

The most recent effort on 1,4-dioxane is an examination of combustion intermediates in its flame using tunable synchrotron photoionization mass spectrometry, by Lin *et al.*[16] Here the observed species arise solely from decomposition of the radicals produced by H-atom abstraction from the 1,4-dioxane, not from its dissociation, and thus this does not directly bear on the present study. However, the decomposition of these radicals is of relevance to the complete modeling of the shock-tube data, and the Lin *et al.* results are again discussed together with that modeling.

An initial consideration of the decomposition based on the likely bond strengths and similarities to the dissociation of cyclohexane,[7,17] and now confirmed by the detailed theory described herein, shows: First, the reaction will not involve a concerted mechanism analogous to 1,3,5-trioxane, leading to the products of (I), as is confirmed by the early signs of chain reaction.[8,9] Second, 1,4-dioxane is able to ring fission at either C–C or C–O bonds with similar barriers. C–O fission can then lead to an exothermic internal abstraction like that seen in cyclohexane where this produces the 'linear' 1-hexene. But here this process generates two distinct long chain species: $HOCH_2CH_2OCHCH_2$, ethylene glycol vinyl ether (EGVE), and $CH_3CH_2OCH_2CHO$, 2-ethoxyacetaldehyde (2EOA), whereas the C–C fission produces a diradical that upon internal abstraction again gives a diradical with the lone pair localized on the terminal CH group, $CH_3OCH_2CH_2OCH$:, which is considerably less stable than EGVE and 2EOA. Furthermore, the barrier to subsequent reaction for $CH_3OCH_2CH_2OCH$: is very high and thus this species may be safely ignored with respect to simulating the experimental data. The two viable long-chain products are now expected to rapidly dissociate by central cleavage to radicals that will drive further chain decomposition. However, it is also possible that EGVE and 2EOA could dissociate *via* tight transition states in retro-ene reactions to form molecular products and this is discussed in the theory section as well as in a forthcoming separate experimental study of EGVE pyrolysis.[18]

As noted above, a complementary theoretical study was conducted to elucidate the important decomposition pathways for 1,4-dioxane. It is also evident from the above comments that dissociation of 1,4-dioxane is complex and neither the theoretical nor experimental work alone would yield a satisfactory, quantitative description of the reaction mechanism. The LS experiments yield accurate initial dissociation rates and provide modeling targets for the later chain reactions whereas the TOF-MS experiments and theory are used primarily to explore the reaction mechanism with theory also providing estimates for some rate coefficients. The results of the experimental and theoretical studies are consistent and are all presented in this paper together with a final suggested mechanism.

## Experimental section

The LS and TOF-MS experiments were performed in a diaphragmless shock tube, DFST, which has been fully described elsewhere.[19] With the DFST, the pressure behind the incident and reflected shock waves, $P_2$ and $P_5$ respectively, can be constrained to very narrow ranges, typically $<\pm 3\%$, over a wide range of temperatures allowing pressure dependant fall off to be clearly resolved.

### DFST/LS

The laser schlieren technique utilizes the deflection of a narrow beam from a He/Ne laser to measure density gradients behind the incident shock wave. The technique has been fully described previously.[20,21] The temperature and pressure behind the incident shock wave are calculated from the incident shock velocity, obtained by interpolation of the time taken for the shock wave to pass adjacent pressure transducers, and the loading conditions, assuming frozen conditions. The uncertainty in velocity is estimated as 0.2%, corresponding to a temperature error of less than 0.5%, here amounting to the order of 10–15 K. The molar refractivity of Kr is 6.367,[22] while that of 1,4-dioxane, 21.65, was calculated from its refractive index and molar density. The usual assumption was made that the mixture molar refractivity does not vary with extent of reaction.

Examples of the raw signal from six varied LS experiments are shown in Fig. 1. In all of these, the large positive spike and preceding negative signal are due to passage of the shock front through the laser beam.[20] The flat level prior to arrival of the incident shock wave at the observation zone is used to establish a baseline in each experiment. The smaller, extended excursion of the signal on the right hand side of the positive spike now represents signal due to chemical reaction. For the higher temperature and pressure experiments, the dissociation is so rapid that the break in the signal can be hard to identify, as in Fig. 1c, e and f. However, it is usually easy to locate this break on a semi-log plot of density gradients derived from the raw data, as shown in Fig. 2 where the individual plots correspond to the respective Fig. 1 examples. Fig. 1b through 1f show an initial positive gradient followed by a negative gradient that dips below the baseline to a minimum before recovering. Such behavior is characteristic of an initial net endothermic process which quickly becomes exothermic. The magnitude and shape of the profile and location of the transition from net positive to negative density gradient are all valuable targets for model development.

### DFST/TOF-MS

The interface between the DFST and TOF-MS consists of a differentially pumped molecular beam sampling system (MBS) that has been described extensively elsewhere along with details of the ionization and analysis cycles.[23] Additionally, some of the TOF-MS experiments were conducted prior to construction of the DFST using the driver section described in

 

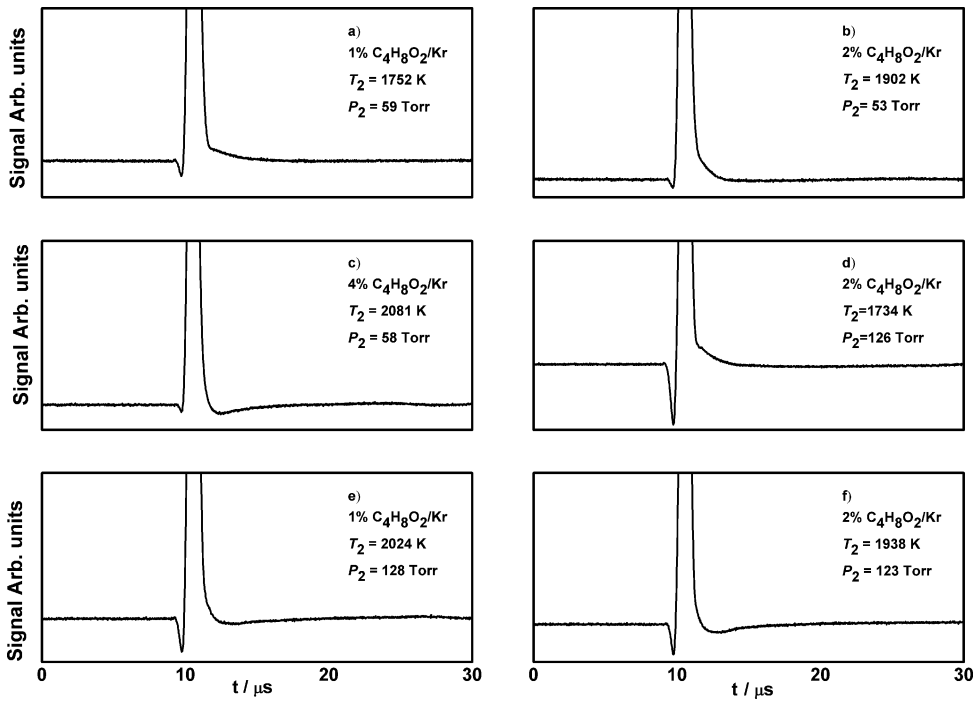


**Fig. 1** Raw laser-schlieren voltage recordings captured in the pyrolysis of 1%, 2% and 4% 1,4-dioxane/Kr mixtures.

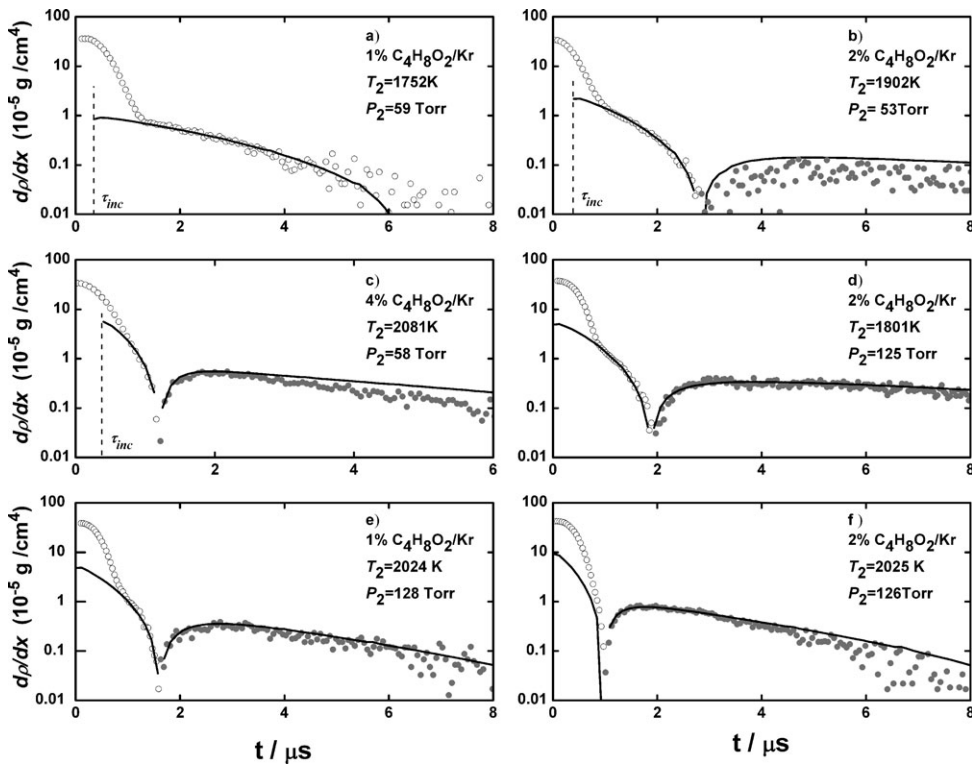


**Fig. 2** Example semilog density gradient plots derived from the raw LS signals of Fig. 1. Absolute values of experimental gradients are plotted, open symbols positive gradients, and closed symbols negative. Lines show the results of simulations using the model of Table 2.

ref. 23. In contrast to the DFST/LS technique where measurements are made behind the incident shock wave, reactions are studied behind the reflected shock wave with the DFST/TOF-MS. The conditions behind the reflected shock wave at the endwall are calculated in a manner similar to that used in the LS experiments. However, to minimize the effects of shock wave attenuation the velocities are measured close to the driven section endwall using a second set of pressure transducers.

Ions were created in the molecular beam eluting from the shock tube by 30 eV electron impact ionization, and ion packets were injected into the flight tube of the TOF-MS at either 9.52 μs intervals, 105 kHz, or 25 μs intervals, 40 kHz. In this investigation no attempt was made to extract kinetic data from the TOF-MS results due to the complexity of 1,4-dioxane dissociation. However, the concentration profiles for 1,4-dioxane from the 105 kHz experiments were simulated with the reaction mechanism presented later in the modeling section. With the higher repetition rates the onset of reaction can be determined more accurately than at the lower sampling rates. The 105 kHz experiments are however complicated by the fact that light ions from one injection event overtake heavier ions from the prior ionization cycle in the drift section of the TOF-MS leading to complex mass spectra that have to be deconvoluted.[23] Furthermore, at the higher sampling frequencies the sensitivity of the multi-channel plate detector had to be reduced to minimize saturation of the detector and thus the quality of the peak shapes for minor, but important species, was reduced. Experiments conducted with the lower sampling rate provide clean, well defined mass spectra from which product species can be identified, even early in the reaction. Consequently, the 105 kHz experiments are used only to provide a test of the reaction mechanism whereas the 40 kHz experiments are used mainly to identify reaction products. In each set of experiments mass spectra were acquired for 1 ms and consist of roughly 300 μs before reflection of the incident shock wave with the remainder representing post shock samples.

Examples of the pre-shock and post shock mass spectra from two 40 kHz experiments are shown in Fig. 3 and 4 for reagent mixtures with 4% and 2% 1,4-dioxane respectively. The pre-shock mass spectra, Fig. 3a and 4a, are consistent with the 70 eV literature mass spectrum of 1,4-dioxane[24] although the lower ionization energies used here create somewhat less fragmentation and the very minor peaks in the literature mass spectrum at $m/z$ 17 and 18 are not seen at all in Fig. 3a and 4a. This could be because they are not created in sufficient numbers at 30 eV and are thus below the detection limit.

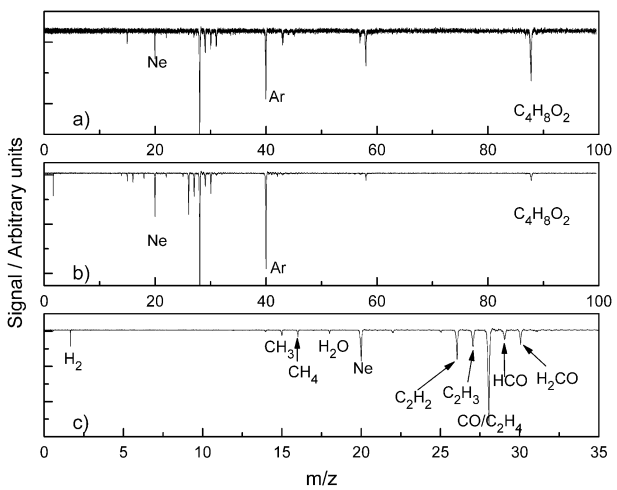


**Fig. 3** Example TOF mass spectra, at 30 eV, from the pre- and post shock regions of a DFST/TOF-MS experiment with 4% 1,4-dioxane dilute in neon. Argon was added to the reagent mixture as an internal standard. Here $T_5$ = 1699 K and $P_5$ = 629 Torr. (a) Pre-shock. (b) Post-shock, 120 μs after reflection of the incident shock wave. (c) expansion of the $m/z$ < 35 region of panel (b).

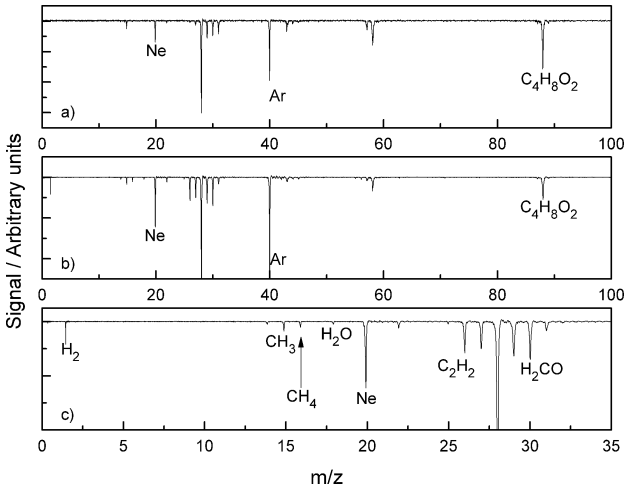


**Fig. 4** Example TOF mass spectra, at 30 eV, from the pre- and post shock regions of a DFST/TOF-MS experiment with 2% 1,4-dioxane dilute in neon. Argon was added to the reagent mixture as an internal standard. The mass spectra from five near identical experiments have been averaged to improve S/N for the minor peaks. $T_5$ = 1461 ± 16 K and $P_5$ = 630 ± 13 Torr. (a) Pre-shock. (b) Post-shock, 200 μs after reflection of the incident shock wave. (c) expansion of the $m/z$ < 35 region of panel (b).

### Reagent mixtures

For the LS experiments mixtures containing 1%, 2% and 4% 1,4-dioxane dilute in krypton were prepared. While for the DFST/TOF-MS experiments the reagent mixtures contained 4% 1,4-dioxane and 4% argon dilute in neon or 2% 1,4-dioxane and 3% argon dilute in neon. All mixtures were prepared manometrically in a 50 L glass vessel that had been evacuated to $<10^{-3}$ Torr. Krypton (AGA 99.999%), was used as supplied. 1,4-Dioxane (Aldrich Chemical Co., 99%) was degassed by repeated freeze–pump–thaw cycles with liquid nitrogen. Reagent mixtures were allowed to homogenize for several hours before use.

## Theoretical methods

The potential energy surface (PES) associated with the decomposition of 1,4-dioxane was explored using single reference and multireference dual level quantum chemistry. The vibrational frequencies and structures of the stationary points and transition states obtained from these calculations are available in the supporting information. The dual level calculations are described using the notation E//G, where E and G denote the quantum chemistry methods used to compute the high-level energies and the low-level geometries and frequencies, respectively. Reliable results for many of the critical points on the dioxane PES were obtained using the single reference QCISD(T)/CBS//B3LYP/6-311++G(d,p) method,[25–27] where the complete basis set (CBS) limit was

estimated using a two point formula[28] and the cc-pVDZ and cc-pVTZ basis sets.[29]

Significant multireference character (as indicated by $Q_1$ diagnostics[30] greater than ~0.02) was found for several important geometries, and in fact the QCISD(T) calculations could not be reliably converged for some species due to multireference contamination. The PES was then further characterized using multireference dual level calculations, where the geometries and frequencies were obtained using multireference perturbation theory[31] (CASPT2), the aug-cc-pVDZ basis set,[32] and a minimal active space of two electrons in two orbitals (2e,2o). High-level multireference energies were calculated at the CASPT2/aug-cc-pVDZ geometries using the CASPT2/CBS method and the (2e,2o) active space. We also briefly considered high level multireference energy calculations at the CASPT2/aug-cc-pVDZ geometries using the Davidson-corrected[33] multireference configuration interaction[34] (MRCI + Q/CBS) method with the (2e,2o) active space and the CASPT2/CBS method with the (6e,6o) active space.

The secondary chemistry for dioxane decomposition was described using a detailed mechanism with rates taken from the literature or estimated, as discussed in detail below. Two sets of theoretical calculations were carried out to refine the detailed mechanism. First, the decomposition pathways of the cyclic radical intermediate 1,4-dioxan-2-yl, $C_4H_7O_2$, were characterized using the G3B3 method.[35] Second, the abstraction rate for OH + dioxane was calculated using variational transition state theory. The abstraction calculations were performed with MPW1K[36] energetics, frequencies, and rotational constants and small curvature tunneling.[37] The MPW1K method was empirically optimized[36] for abstraction reactions for the 6-31+g(d,p) basis set. The state densities were evaluated using the harmonic oscillator-rigid rotor approximations, with a one-dimensional anharmonic correction for the HO-dioxane torsion at the transition state. The kinetic effect of the prereactive van der Waals wells (which should be negligible at elevated temperatures) was not included in the present treatment.

The B3LYP geometry optimizations and G3B3 and MPW1K calculations were carried out using Gaussian,[38] and the QCISD(T), MRCI, and CASPT2 calculations were carried out using Molpro.[39]

## Theoretical results

The results of the single reference and multireference dual level calculations are presented in Table 1. The accuracy of the single reference QCISD(T)/CBS method is expected to be similar to that of the widely used CCSD(T)/CBS method, with $1\sigma$ uncertainties of only ~2 kcal/mol when single reference methods are appropriate. The reliability of the CASPT2/CBS multireference calculations is less well understood. We therefore tested two other dual-level multireference methods. The use of a larger active space, (6e,6o), which might be more suitable for characterizing some of the concerted bond breaking/H-transfer events considered here, did not significantly change the predicted CASPT2/CBS barrier heights and relative energies, with differences of only 2–4 kcal/mol for the 1,4-dioxane ring opening saddle points. The MRCI + Q method with the (2e,2o) active space predicted significantly different energetics than CASPT2, with differences in the predicted energies of the ring opening saddle points of up to 16 kcal/mol. This may indicate errors associated with size extensivity and that Davidson's size extensivity correction is not reliable for a system as large as dioxane when such a small active space is used.[40] The neglect of Davidson's correction did not improve agreement between the CASPT2 and MRCI results. For example, the single reference saddle point energy for ring opening to EGVE (SP1) is 78.5 kcal/mol, with a $Q_1$ diagnostic of 0.02, suggesting that the single reference calculation should be fairly reliable. The CASPT2 energy is 75.8 kcal/mol in fair agreement with the single reference result, whereas the MRCI + Q energy is significantly higher (87.2 kcal/mol). Neglecting the Davidson correction gives 94.2 kcal/mol for the energy of SP1. Clearly, the results of the multireference calculations may be assigned uncertainties of several kcal/mol. We focus on the CASPT2 results because they more closely reproduce the QCISD(T) results for species where the $Q_1$ diagnostic is small and because the CASPT2 calculations are less computationally demanding than the MRCI ones, allowing for a more complete characterization of the PES.

For species with $Q_1$ diagnostics less than ~0.02, the QCISD(T) method may be expected to be more reliable than

**Table 1** Labels, names, zero point inclusive energies (kcal/mol), and multireference $Q_1$ diagnostics for stationary points on the 1,4-dioxane potential energy surface[e]

| Label | Species name | $SR$[a] | $MR$[b] | $Q_1$[c] |
|---|---|---|---|---|
| R | 1,4-dioxane ($C_{2h}$) | **0.0** | 0.0 | 0.012 |
| R′ | 1,4-dioxane ($D_2$) | **6.1** | | 0.011 |
| EGVE | $CH_2CHOCH_2CH_2OH$ | **6.2** | 4.5 | 0.012 |
| 2EOA | $CH_3CH_2OCH_2CHO$ | **–1.0** | –4.0 | 0.013 |
| C3a | $CH_3OCH_2CH_2OCH$ | **66.5** | | 0.016 |
| MOP | $CH_3OCH_2CH_2CHO$ | **–1.1** | | 0.013 |
| D1 | $\cdot CH_2CH_2OCH_2CH_2O\cdot$ | [d] | **82.3** | |
| D2 | $\cdot CH_2OCH_2CH_2OCH_2\cdot$ | 81.1 | **75.0** | 0.025 |
| P1 | $CH_2CHO + CH_2CH_2OH$ | **72.3** | | 0.023, 0.011 |
| P2 | $CH_2CHO + CH_3CH_2O$ | **78.9** | | 0.023, 0.017 |
| P3 | $CH_2CHO + CH_3OCH_2$ | **78.1** | | 0.023, 0.018 |
| P4 | $2\ CH_2O + CH_2CH_2$ | **33.3** | | 0.016, 0.011 |
| P5 | $CH_3CHO + CH_2CHOH$ | **5.1** | | 0.015, 0.013 |
| P6 | $H + cC_4O_2H_7$ | **96.3** | | 0.000, 0.016 |
| P7 | $H_2 + cC_4O_2H_6$ | **22.9** | | 0.006, 0.014 |
| | $[R \rightleftarrows R']^{\dagger}$ | 10.7 | | 0.011 |
| SP1 | $[R \rightleftarrows EGVE]^{\dagger}$ | 78.5 | **75.8** | 0.022 |
| SP2 | $[R \rightleftarrows 2EOA]^{\dagger}$ | [d] | **84.4** | |
| SP3a | $[R \rightleftarrows C3a]^{\dagger}$ | **86.5** | 85.3 | 0.017 |
| SP3b | $[C3a \rightleftarrows MOP]^{\dagger}$ | 111.3 | **116.9** | 0.023 |
| SP4 | $[R \rightleftarrows P4]^{\dagger}$ | **92.9** | | 0.015 |
| SP5 | $[EGVE \rightleftarrows P5]^{\dagger}$ | **54.0** | 47.3 | 0.020 |
| SP6 | $[2EOA \rightleftarrows P5]^{\dagger}$ | **54.3** | 46.5 | 0.015 |
| SP7 | $[R \rightleftarrows P7]^{\dagger}$ | **111.8** | | 0.016 |
| SP1′ | $[R' \rightleftarrows EGVE]^{\dagger}$ | 83.9 | **84.2** | 0.033 |
| SP2′ | $[R' \rightleftarrows 2EOA]^{\dagger}$ | [d] | **84.4** | |
| SPD1 | $[R \rightleftarrows D1]^{\dagger}$ | [d] | **84.8** | |
| SPD2 | $[R \rightleftarrows D2]^{\dagger}$ | 85.7 | **76.0** | 0.023 |
| SP1* | $[D1 \rightleftarrows EGVE]^{\dagger}$ | [d] | **85.0** | |
| SP2* | $[D1 \rightleftarrows 2EOA]^{\dagger}$ | [d] | **84.1** | |
| SP3a* | $[D2 \rightleftarrows C3a]^{\dagger}$ | **84.4** | 82.7 | 0.018 |

[a] Single reference QCISD(T)/CBS//B3LYP/6-311++G(d,p). [b] Multireference CASPT2/CBS//CASPT2/aug-cc-pVDZ. [c] $Q_1$ diagnostic from the QCISD/cc-pVTZ calculation. [d] The SR calculation could not be reliably converged. [e] Vibrational frequencies and structures for the stationary points are available in the supporting information.

the CASPT2 calculations. The multireference method is in principle more accurate than the single reference approach when the $Q_1$ diagnostic is large, but the size of 1,4-dioxane limits the active spaces that can be affordably used in the multireference calculations and consequently limits their accuracy. We note that energies obtained using the QCISD(T) method can be surprisingly accurate even when the $Q_1$ diagnostic is large.[41]

To construct a composite PES, we chose to use the single reference values if the $Q_1$ diagnostic was less than 0.02 and if the calculation could be reliably converged. If not, the (2e,2o)-CASPT2/CBS results were used. When mixing the results of different electronic structure methods, reference structures must be chosen at which to join the calculated surfaces. Here we chose the $C_{2h}$ structure of 1,4-dioxane as our reference for every decomposition channel, as we are primarily interested in the energetics and kinetics of the ring-opening step. The resulting composite PES is shown in Fig. 5.

1,4-dioxane has two stable conformers. The "chair" ($C_{2h}$) conformer is lower in energy than the "twist" ($D_2$) conformer by 6 kcal/mol, and the two conformers are separated by an 11 kcal/mol barrier relative to the chair conformer, Table 1. These structures are analogous to those found for 1,3-dioxane,[42] cyclohexane,[43] and other saturated six-membered rings.

Several saddle points associated with transition states for ring opening were identified. The ring may open at a C–O bond accompanied by an H atom transfer from either carbon β to the distant atom in the breaking bond resulting in either EGVE or 2EOA as shown schematically in reactions (1) and (2).

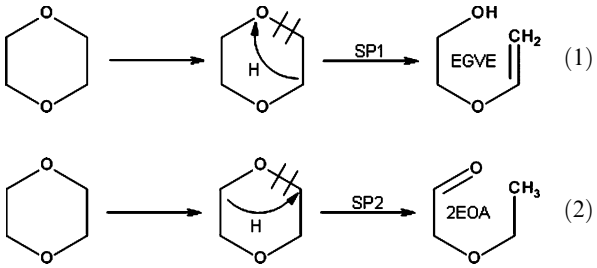


For reactions (1) and (2), we further distinguish saddle points for the chair (SP1 and SP2) and twist (SP1′ and SP2′) forms of 1,4-dioxane in Table 1. The ring can also open at a

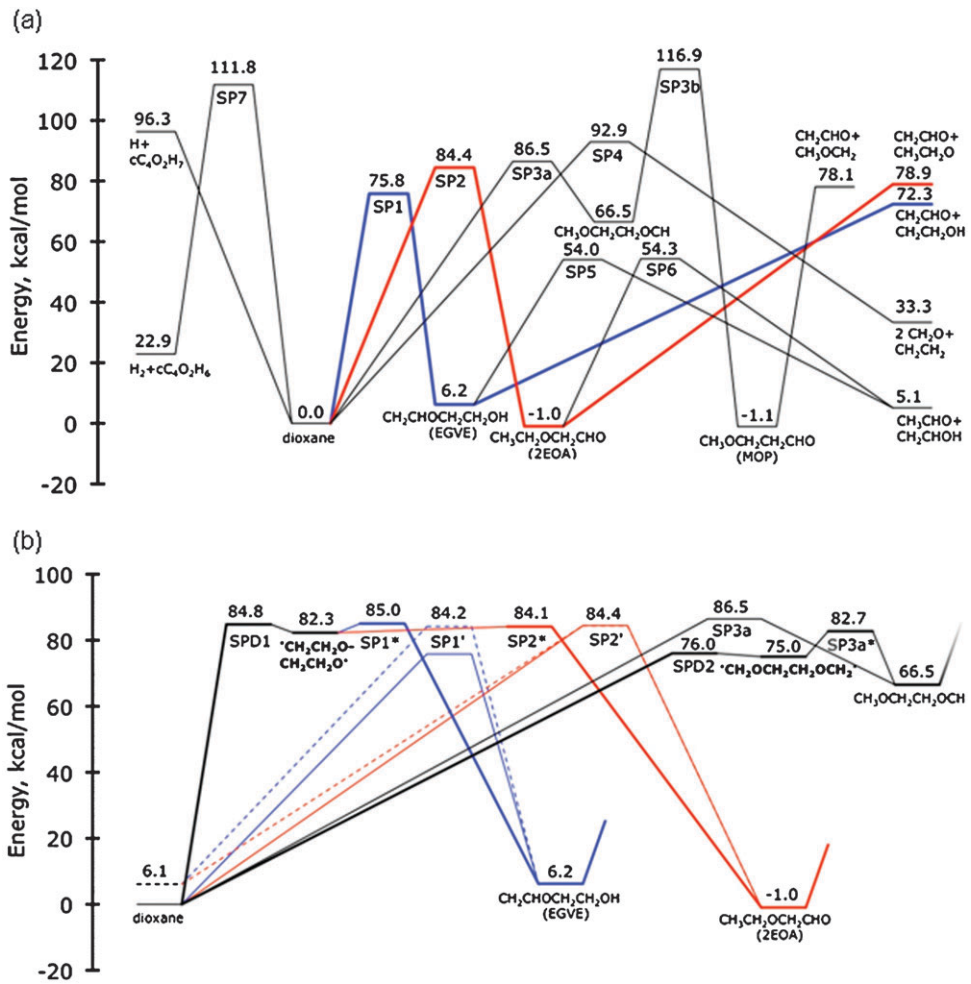


**Fig. 5** Composite potential energy diagram for 1,4-dioxane decomposition, showing (a) an overview of the major decomposition pathways and (b) a highlight of the ring opening pathways, including those involving the diradical intermediates (bold) and the twist conformer of dioxane (dashed). The thin solid lines in (b) reproduce the SP1, SP2, and SP3a pathways shown in (a). The dominant decomposition pathways *via* EGVE and 2EOA are shown as blue and red, respectively.

 

C–C bond accompanied by an H atom transfer across the opening bond, giving an intermediate, C3a, that is ~60 kcal/mol higher in energy than EGVE and 2EOA. This intermediate may subsequently isomerize to a more stable species, methoxypropanal (MOP) however the barrier remains ~53 kcal/mol higher than C3a, Fig. 5.

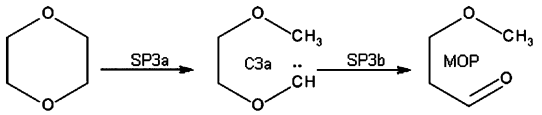

(3)

SP4 is a saddle point for dioxane decomposition involving the concerted breaking of 3 bonds, two C–O bonds and one C–C bond, giving the same products as reaction (I) but by a very different mechanism to that suggested by Battin *et al.*[9]

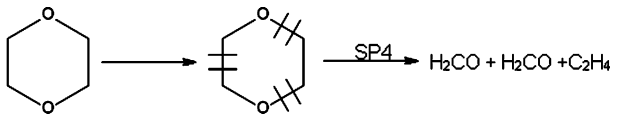

(4)

SP3a and SP4 are associated with the chair ($C_{2h}$) form of dioxane, and no distinct saddle points associated with the $D_2$ form were found.

The molecules EGVE, 2EOA, and MOP can easily decompose *via* cleavage of the central bond. For $HOCH_2CH_2OCHCH_2$ (EGVE) and $CH_3CH_2OCH_2CHO$ (2EOA) this may involve a prior H atom transfer (SP5 and SP6, respectively) leading to $CH_3CHO$ + $CH_2CHOH$, or more easily, with no H-atom transfer and little barrier, to give two radicals, as in reactions (6) and (8).

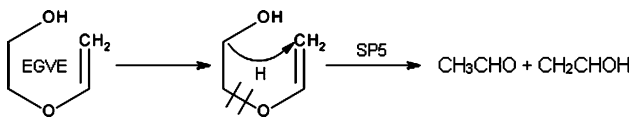

(5)

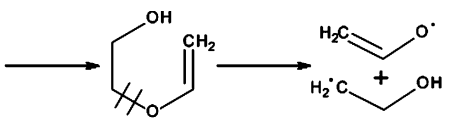
(6)

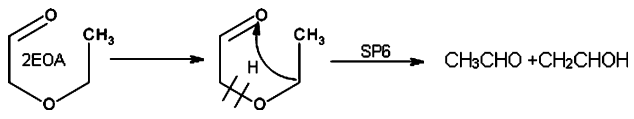

(7)

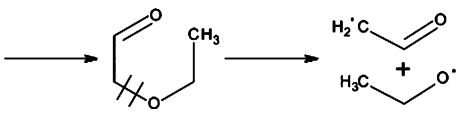
(8)

The product radicals of reactions (6) and (8) will themselves dissociate readily to smaller radicals. This is considered in detail in the later discussion of modeling of the LS experiments.

The lowest barrier for decomposition of $CH_3OCH_2CH_2CHO$ (MOP) is through reaction (9) by scission of the central C–C bond.

$$CH_3OCH_2CH_2CHO \rightarrow CH_2CHO + CH_3OCH_2 \quad (9)$$

However, the high barrier in SP3b, Fig. 5, makes formation of MOP unlikely and it is not included in the final modeling. We note that the loss of $H_2$ *via* reaction (10) from 1,4-dioxane and the barrierless loss of H by reaction (11) can occur only at high energies and are also likely minor processes in the present system.

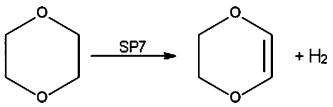

(10)

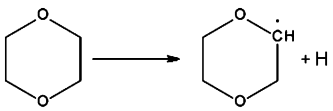

(11)

The ring opening processes discussed above, reactions (1)–(4), describe concerted mechanisms where an H atom transfer accompanies the ring opening (SP1, SP2, and SP3a) or where three bonds are broken nearly simultaneously (SP4). As discussed previously for cyclohexane,[7] such processes may also occur *via* step-wise pathways involving diradical[17] intermediates. Pathways for 1,4-dioxane decomposition involving diradical intermediates are shown in Fig. 5(b). There are two such diradicals, D1 and D2, that are formed *via* SPD1 and SPD2 respectively.

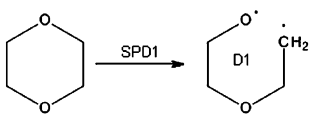

(12)

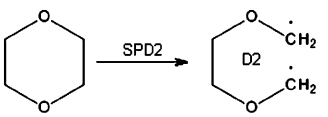

(13)

D1 and D2 are both high-energy structures that are weakly bound, and are formed *via* loose saddle points with small reverse barriers. The diradical D1 may subsequently transfer H-atoms *via* loose, shallow barriers to give either EGVE, reaction (14), or 2EOA, reaction (15).

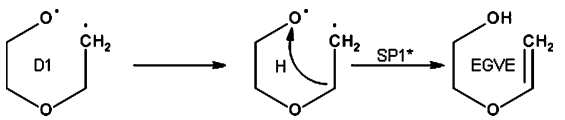

(14)

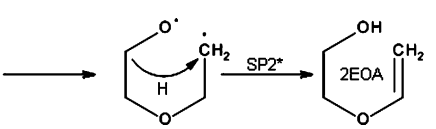

(15)

Reaction (12) followed by either reactions (14) or (15) is the step-wise analog of reaction (1) or (2), and, as seen in Fig. 5(b), the step-wise and concerted mechanisms have

similar energetics. Thus the results of these two steps are the same as reactions (1) and (2) and may be lumped together with these in a model. Similarly, the diradical D2 may form C3a by an H-atom transfer through saddle point SP3*. However, this occurs at energies similar to formation of C3a by the concerted mechanism shown in reaction (3) and is thus also not considered in modeling the LS experiments. D1 and D2 can also fragment to give 2 $CH_2O$ + $C_2H_4$, and these processes are multistep analogs of reaction (4). However, the barriers for fragmentation are estimated to be at least 20 kcal/mol larger than the barriers for the H-atom transfer reactions (14)–(16), and the fragmentation pathways of D1 and D2 are not shown in Fig. 5.

**Table 2** Reaction mechanism and Arrhenius parameters for 1,4-dioxane pyrolysis at 120 Torr. Units: kcal, mole, $cm^3$, s

| Reaction | | log*A* | *n* | $E_a$ | $\Delta H_{r,298K}$ | Ref. |
|---|---|---|---|---|---|---|
| $R_1$ | $C_4H_8O_2 = CH_2CH_2OH + CH_2CHO$ | 55.550 | −12.72 | 78.8 | 72.0 | this work |
| $R_2$ | $C_4H_8O_2 = CH_2CHO + CH_3CH_2O$ | 55.650 | −12.72 | 78.4 | 75.0 | this work |
| $R_3$ | $C_2H_4 + OH = CH_2CH_2OH$ | 35.538 | −7.78 | 5.0 | −27.8 | 58 |
| $R_4$ | $CH_3CH_2O = CH_3 + CH_2O$ | 10.745 | 0.00 | 15.5 | 13.4 | 59 |
| $R_5$ | $CH_3CH_2O = H + CH_3CHO$ | 10.225 | 0.00 | 15.5 | 15.6 | est. from ref. 45 |
| $R_6$ | $CH_2CHO = CH_3 + CO$ | 32.938 | −6.57 | 44.3 | −5.6 | 44 |
| $R_7$ | $CH_2CHO = CH_2CO + H$ | 30.551 | −5.86 | 46.1 | 37.5 | 44 |
| $R_8$ | $CH_2CO + H = CH_3 + CO$ | 8.890 | 1.45 | 2.8 | −61.9 | 44 |
| $R_9$ | $H + CH_2CHO = CH_3 + HCO$ | 13.300 | 0.00 | 0.0 | −10.0 | 60 |
| $R_{10}$ | $H + CH_2CHO = CH_2CO + H_2$ | 13.000 | 0.00 | 0.0 | −66.8 | 60 |
| $R_{11}$ | $CH_3 + CH_2O = HCO + CH_4$ | 1.502 | 3.36 | 4.3 | −16.9 | 15 |
| $R_{12}$ | $H + C_4H_8O_2 = H_2 + C_4H_7O_2$ | 5.650 | 2.30 | 2.0 | −7.9 | est. see text |
| $R_{13}$ | $OH + C_4H_8O_2 = C_4H_7O_2 + H_2O$ | 7.300 | 1.80 | 0.0 | −22.6 | est. see text |
| $R_{14a}$ | $C_4H_7O_2 = HCO + CH_2O + C_2H_4$ | 15.800 | −2.00 | 23.0 | 27.8 | est. |
| $R_{14b}$ | $C_4H_7O_2 = CH_3CH_2O + CH_2CO$ | 8.900 | 0.00 | 23.0 | 27.8 | est. |
| $R_{15}$ | $HCO + M = H + CO + M$ | 17.681 | −1.20 | 17.7 | 15.6 | 57 |
| $R_{16}$ | $H + HCO = H_2 + CO$ | 13.850 | 0.00 | 0.0 | −88.6 | 41 |
| $R_{17}$ | $H + CH_2O = H_2 + HCO$ | 7.759 | 1.90 | 2.7 | −16.1 | 63 |
| $R_{18}$ | $HCO + HCO = CH_2O + CO$ | 13.031 | 0.00 | 0.0 | −72.6 | 0.5 × rate in ref. 57 |
| $R_{19}$ | $CH_2O + M = H + HCO + M$ | 36.100 | −5.50 | 93.9 | 88.2 | 61 |
| $R_{20}$ | $CH_2O + M = H_2 + CO + M$ | 38.640 | −6.10 | 93.9 | −0.5 | 61 |
| $R_{21}$ | $CH_3 + HCO = CH_4 + CO$ | 16.800 | −1.23 | 0.5 | −89.5 | 41 |
| $R_{22}$ | $OH + CH_2CHO = CH_2OH + HCO$ | 13.500 | 0.00 | 0.0 | −6.0 | 60 |
| $R_{23}$ | $OH + CH_2CHO = CH_2CO + H_2O$ | 13.000 | 0.00 | 0.0 | −81.4 | 60 |
| $R_{24}$ | $OH + CH_2CO = CH_2OH + CO$ | 13.000 | 0.00 | 0.0 | −27.8 | est. from ref. 62 |
| $R_{25}$ | $OH + CH_2O = HCO + H_2O$ | 7.893 | 1.63 | −1.0 | −30.7 | 63 |
| $R_{26}$ | $OH + HCO = H_2O + CO$ | 13.700 | 0.00 | 0.0 | −103.3 | 60 |
| $R_{27}$ | $OH + CO = H + CO_2$ | 6.800 | 1.50 | −0.5 | −21.7 | 64 |
| $R_{28}$ | $OH + CH_4 = CH_3 + H_2O$ | 13.757 | 0.00 | 8.2 | −13.8 | 65 |
| $R_{29}$ | $OH + C_2H_4 = C_2H_3 + H_2O$ | −0.884 | 4.2 | 0.8 | −7.9 | 58 |
| $R_{30}$ | $OH + CH_3 = CH_2(T) + H_2O$ | 4.620 | 2.57 | 4.0 | −8.3 | 66 |
| $R_{31}$ | $OH + CH_3 = CH_2(S) + H_2O$ | 12.570 | 0.00 | 0.0 | 0.7 | 66 |
| $R_{32}$ | $OH + CH_3 = CH_2OH + H$ | 9.782 | 1.00 | 3.2 | 4.0 | 66 |
| $R_{33}$ | $OH + CH_3 = HCOH + H_2$ | 12.040 | 0.00 | 0.0 | −13.8 | 66 |
| $R_{34}$ | $CH_3OH + M = CH_3 + OH + M$ | 15.748 | 0.00 | 61.6 | 92.1 | 67 |
| $R_{35}$ | $OH + H + M = H_2O + M$ | 20.500 | −1.53 | 0.4 | −118.9 | 68 |
| $R_{36}$ | $CH_2OH = CH_2O + H$ | 22.746 | −3.91 | 36.2 | 30.2 | est. |
| $R_{37}$ | $HCOH + M = HCO + H + M$ | 16.040 | 0.00 | 34.1 | 32.0 | est. |
| $R_{38}$ | $OH + C_2H_3 = C_2H_2 + H_2O$ | 12.700 | 0.00 | 0.0 | −83.8 | 60 |
| $R_{39}$ | $OH + C_2H_2 = CH_2CO + H$ | 5.500 | 1.92 | 0.6 | −22.6 | 69 |
| $R_{40}$ | $OH + C_2H_2 = CH_3 + CO$ | 7.880 | 1.05 | 1.1 | −54.7 | 69 |
| $R_{41}$ | $OH + H_2 = H_2O + H$ | 13.513 | 0.00 | 6.4 | −14.7 | 70 |
| $R_{42}$ | $OH + C_2H_6 = C_2H_5 + H_2O$ | 13.820 | 0.00 | 5.0 | −18.1 | 70 |
| $R_{43}$ | $CH_3 + C_4H_8O_2 = C_4H_7O_2 + CH_4$ | 12.300 | 0.00 | 12.5 | −8.8 | est. |
| $R_{44}$ | $CH_3CHO = CH_3 + HCO$ | 59.151 | −13.05 | 102.4 | 84.9 | 71 |
| $R_{45}$ | $CH_3CHO = CH_4 + CO$ | 58.370 | −13.05 | 102.4 | −4.5 | 71 |
| $R_{46}$ | $H + CH_3CHO = CH_2CHO + H_2$ | 3.433 | 3.10 | 5.2 | −9.4 | 71 |
| $R_{47}$ | $H + CH_3CHO = CH_3 + CO + H_2$ | 5.100 | 2.58 | 1.2 | −3.8 | 71 |
| $R_{48}$ | $OH + CH_3CHO = CH_2CHO + H_2O$ | 13.200 | 0.00 | 2.0 | −24.0 | est. |
| $R_{49}$ | $OH + CH_3CHO = CH_3 + CO + H_2O$ | 10.350 | 0.74 | −1.1 | −18.4 | 60 |
| $R_{50}$ | $H + CH_2OH = CH_2O + H_2$ | 13.000 | 0.00 | 0.0 | −74.0 | 60 |
| $R_{51}$ | $CH_2CO + M = CH_2(T) + CO + M$ | 15.350 | 0.00 | 57.6 | 78.7 | 72 |
| $R_{52}$ | $C_2H_5OH + H = CH_2CH_2OH$ | 34.538 | −7.78 | 5.0 | 28.5 | est. from ref. 45 |
| $R_{53}$ | $OH + C_2H_4 = C_2H_3OH + H$ | 4.200 | 2.56 | 4.1 | 0.8 | 58 |
| $R_{54}$ | $H + C_2H_3OH = CH_2CHO + H_2$ | 13.000 | 0.00 | 0.0 | −19.2 | est. |
| $R_{55}$ | $C_2H_3OH = CH_3 + HCO$ | 59.151 | −13.05 | 102.4 | 75.0 | est. |
| $R_{56}$ | $OH + CH_2OH = CH_2O + H_2O$ | 13.380 | 0.00 | 0.0 | −88.7 | 73 |
| $R_{57-83}$ | $C_2H_6 + M = CH_3 + CH_3 + M$ | 64.945 | −12.78 | 111.7 | 90.2 | *See a* |

[a] Sub-mechanism for recombination of methyl radicals taken from references.[48,51]



 

Preliminary master equation calculations were carried out for the ring opening of 1,4-dioxane using the composite PES discussed above. In agreement with the experimental results, the formation of C3a and 2 $CH_2O$ + $CH_2CH_2$ *via* SP4 is found to be small (<1%), and formation of EGVE and 2EOA are the two major channels. The results of the master equation calculations were very sensitive to the treatment of the transition states for ring opening to the diradical (SPD1) and subsequent isomerization (SP1* and SP2*). This region of the potential energy surface is characterized by several low frequency torsional and bending motions, and these processes are therefore not well described by the usual harmonic oscillator state counts. A more rigorous anharmonic treatment was not pursued. Due to the large uncertainties in the estimated rate coefficients for formation of EGVE and 2EOA, we did not attempt to fit the results of master equation calculations to the experimental results. Instead, the theoretical values provided initial estimates that were further optimized iteratively during development of the model presented in Table 2. The master equation calculations suggest that multiple mechanisms for ring opening likely contribute to the formation of EGVE and 2EOA. Roughly half of the ring opening events proceed *via* the diradical intermediate D1, which subsequently forms EGVE and 2EOA in nearly equal amounts. The remaining decomposition of 1,4-dioxane proceeds *via* both the chair and twist concerted pathways, which favor formation of EGVE and 2EOA, respectively. In the modeling discussed below, a single rate was associated with the formation of each initial product EGVE and 2EOA, and no attempt was made to quantify the relative importance of the multiple mechanisms for ring opening. The results of the master equation analyses and a comparison of the experimental and theoretical rate coefficients are available in the supporting information. Due to the uncertainties in the calculations, the experimental rate coefficients are preferred and are presented in detail below. The results of the theoretical study are predominantly used to guide development of the reaction mechanism by exploring pathways that cannot be isolated in the current experiments.

## Experimental results and discussion

### TOF-MS

Ten shock tube TOF-MS experiments on the pyrolysis of 4% 1,4-dioxane dilute in neon were performed over 1400–1800 K and pressures of 500–700 Torr using the older driver section with Mylar diaphragms. An additional twenty three experiments were performed at similar temperatures and pressures close to 620 Torr with a 2% reagent mixture and the DFST. Over the experimental range the same species were observed in all experiments with the primary differences being changes in the rates of formation and consumption of species with respect to temperature. Due to small electron impact ionization cross sections and low concentrations of species such as $CH_3$, $CH_4$ and $H_2O$, Fig. 3 and 4, it was not possible to obtain quantitative concentration/time profiles for these mechanistically important species. Consequently, the following discussion considers only their implication for the decomposition mechanism of 1,4-dioxane and the comments apply to all the TOF-MS experiments, although only the experiment of Fig. 3 is used to illustrate the discussion.

For the example experiment shown in Fig. 3 it is clear that almost all of the 1,4-dioxane has been consumed in the first 120 μs of reaction, and the peaks in the post-shock mass spectrum, Fig. 3b and c, therefore represent products and not fragments of the parent molecule. In Fig. 3c the product peaks are assigned to $H_2$, $CH_3$, $CH_4$, OH, $H_2O$, $C_2H_2$, $C_2H_3$, $C_2H_4$, CO, HCO and $H_2CO$. Of these, there are five that are of particular value to understanding the dissociation mechanism of 1,4-dioxane: $CH_3$, $CH_4$, $H_2$, OH and $H_2O$. The $m/z$ for these cannot be generated by fragmentation of any of the higher mass products in the ion source. The $H_2O$ peak is quite weak and $m/z$ 17 is barely noticeable in Fig. 3c. It is possible that the $m/z$ 18 peak is due to background water in the ion source, however, blank runs show no indication of water in the post shock mass spectra. Thus $H_2O$ must be formed during reaction and the most likely source is from abstraction of H-atoms by OH radicals. Such reactions are typically very fast leading to low concentrations of OH and the observed mass spectra indicate that these are near the detection limit of the current apparatus. The $CH_3$ peak could be a fragment of $CH_4$ but it is also likely, based on the relative peak heights and 30 eV ionization energy, that at least part of the peak is due to $CH_3$ radicals being ionized in the molecular beam.

The molecules $H_2$, $H_2O$ and $CH_4$ are likely formed by reactions involving abstraction of H-atoms from other molecules by H, OH and $CH_3$ radicals. Thus a mechanism for 1,4-dioxane pyrolysis must generate these species. A potential source of these is ethylene glycol vinyl ether, $CH_2CHOCH_2CH_2OH$, the immediate product from dissociation of 1,4-dioxane *via* SP1. EGVE can decompose to vinoxy radical, $CH_2CHO$, and, $CH_2CH_2OH$ *via* reaction (6). This will then be followed by dissociation of the vinoxy radical, by two routes, forming H + $CH_2CO$ or $CH_3$ + CO,[44] whereas $CH_2CH_2OH$ dissociates predominantly to OH + $C_2H_4$.[45] The other long-chain species, 2-ethoxyacetaldehyde, can decompose by reaction (8) and will again form vinoxy and now also $CH_3CH_2O$. This latter species is again expected to readily dissociate, mainly to $CH_2O$ + $CH_3$.[45] Thus, from dissociation of 1,4-dioxane *via* SP1 and SP2, a pool of radicals can be developed that are consistent with the TOF-MS results, one which can recombine exothermically, and one which will also propagate a chain reaction without relying on the thermal dissociation of formaldehyde. From the mass spectra crude estimates of the branching ratio between reactions (1) and (2) can be obtained by consideration of the ratios $[C_2H_4]/[H_2CO]$ and $[CH_4]/[H_2O]$, assuming that each species can ultimately be associated with either reaction (1) or (2). These estimates yield a branching ratio of $k_1/(k_1+k_2) = 0.45 \pm 0.1$.

### LS

Seventy seven LS experiments with 1, 2 and 4% 1,4-dioxane dilute in krypton were performed over the range $1600 < T_2 < 2100$ K for pressures around 56 and 123 Torr. The 4% mixture was used only at $P_2 = 58 \pm 3$ Torr. At high temperatures or pressures the early density gradients are steeply falling and soon negative rendering difficult the determination of $(d\rho/dx)$

for $t_0$, the time origin at the onset of reaction, and extrapolation to this was assisted by detailed modeling of the entire process. Experiments were performed with the 1% mixtures at $P_2 = 58 \pm 1$ Torr and $123 \pm 3$ Torr and with the 2% mixtures at $P_2 = 54 \pm 3$ Torr and $123 \pm 2$ Torr. Again, the first few points of each semi-log density gradient plot in Fig. 2 are from the end portion of the shock front/laser-beam interaction described above. Unfortunately, this interaction masks the location of $t_0$. Consequently, $t_0$ was located by a well established analysis of this signal.[46] In most cases the time origin is then believed to be located to an accuracy of 0.1–0.2 μs.

The modeling of the 56 Torr experiments consistently runs parallel to the experimental data on the underside. The difference was larger than could be assigned to error in the location of $t_0$ and simple adjustment of rate coefficients did not improve the simulation. This situation is typically indicative of a small incubation delay[47,48] and the low pressure simulations have accordingly been delayed by $\sim$0.3 μs as indicated in Fig. 2a–c.

In none of the LS experiments was there any trace of an increase in the measured density gradient past $t_0$; the gradient profiles are all monotonically decreasing down to the late negative minimum. This situation is in sharp contrast to that in cyclohexane[7] where rising early positive gradients are often apparent. In the terms used in that work, the present process is clearly a "one-step" reaction with immediate dissociation of the initial products EGVE and 2EOA *via* reactions (6) and (8) above. Of course the initial reactions, (1) and (2), are near thermoneutral and cannot by themselves generate the observed large positive gradients. The rate is indeed controlled by (1) and (2), but the enthalpy of reaction arises from reactions (6) and (8), and to a lesser extent the decomposition of the radicals formed therein. Consequently, the mechanism of Table 2 combines reactions (1) and (6) into reaction ($R_1$) and (2) and (8) into reaction ($R_2$).

The gradients were also completely modeled to allow for minor contributions from additional radical decomposition in the initial gradients (see below). An effective total dissociation rate constant for the initial decomposition of 1,4-dioxane is finally obtained from the density gradient extrapolated to $t_0$ assuming that EGVE and 2EOA are formed in the above 45 : 55 ratio. These molecules then dissociate immediately as do the product radicals $CH_3CH_2O$ and $CH_2CH_2OH$, leaving the effective $\Delta H$ of initial reaction near 80 kcal/mol. The sensitivity of the simulations to variation in the total initial rate and the branching ratio is shown in Fig. 6 and 7 respectively.

The total composite dissociation rates, $k_1+k_2$, ultimately obtained by the above procedures are shown in Fig. 8. For the lower temperature and pressure experiments, *e.g.* those of Fig. 2a, the extrapolation is rather obvious and quite accurate, and subsequent refinement of an initial estimate through simulation of the complete density gradient profile typically results in a $<10\%$ change in the trial estimate for $k_1+k_2$. For the higher temperature experiments determining the density gradient at $t_0$ is more difficult due to the steep slope of the early part of the data and the initial rate coefficients are best determined through simulation of the complete LS profile.

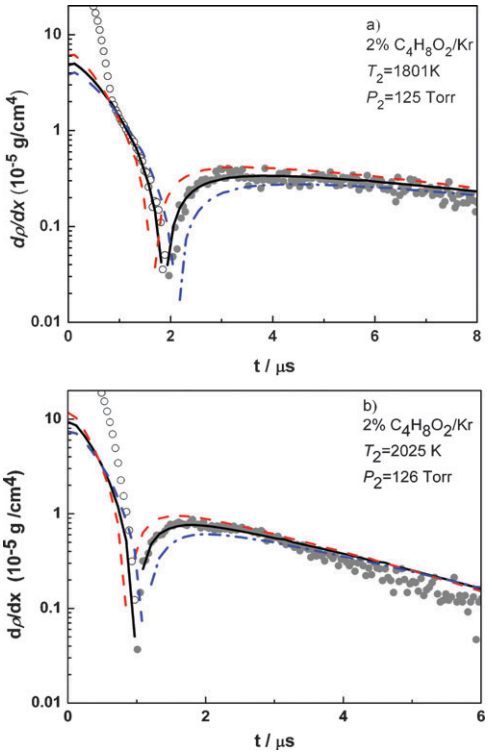


**Fig. 6** Sensitivity of the modeling results to the value of $(k_{R1}+k_{R2})$ the initial dissociation of 1,4-dioxane. The branching between reaction *via* SP1 and SP2 has been fixed at the 45 : 55 and only the total rate coefficient varied. Absolute values are plotted. Symbols represent experimental data with open symbols corresponding to positive density gradients and closed symbols to negative ones. Lines are the results of simulations. Solid black line, model in Table 2. Red dashed line, model in Table 2 but with $(k_{R1}+k_{R2}) \times 1.3$. Blue dash-dot line, model in Table 2 but with $(k_{R1}+k_{R2}) \times 0.7$.

However, even in these cases the initial estimates rarely change by more than 10–15%. The $k_1+k_2$ shown in Fig. 8 have been individually fit to the following modified Arrhenius expressions over the range 1600–2100 K, holding $k_1/(k_1+k_2) = 0.45$.

$$k_1 + k_2\,(123\ \text{Torr}) = (1.58 \pm 0.5) \times 10^{59} \times \text{T}^{-13.63} \times \exp(-43970/\text{T})\ \text{s}^{-1}$$

$$k_1 + k_2\,(56\ \text{Torr}) = (3.16 \pm 1.1) \times 10^{79} \times \text{T}^{-19.13} \times \exp(-51326/\text{T})\ \text{s}^{-1}$$

As discussed in the theory section ambiguities associated with low frequency internal rotors at the diradical transition states preclude quantitative theoretical predictions of $k_1$ and $k_2$. However, master equation calculations carried out using the PES in Fig. 5 are nonetheless consistent with the experimental rates reported above and the measured rates are most likely composites of contributions from more than one dissociation pathway as discussed in the theory section. A comparison of the master equation results and the experimental data is given in the supporting information.

### Modeling of LS experiments

Simulations of the LS experiments were performed using the mechanism of Table 2 in a computer code designed for ideal

 

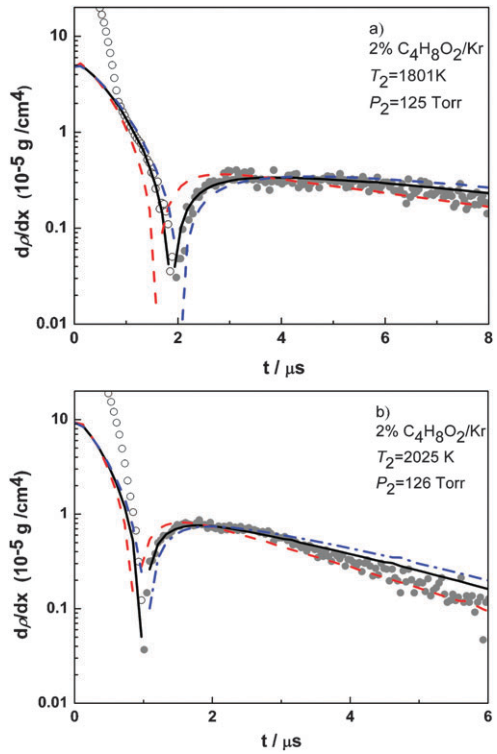


**Fig. 7** Sensitivity of the modeling results to the value of the branching ratio between dissociation of 1,4-dioxane *via* SP1 and SP2, $\phi = k_{R1}/(k_{R1}+k_{R2})$. Here the initial total rate of dissociation of 1,4-dioxane has been fixed. Absolute values are plotted. Symbols represent experimental data with open symbols corresponding to positive density gradients and closed symbols to negative ones. Lines are the results of simulations. Solid black line, model in Table 2, $\phi = 0.45$. Red dashed line, $\phi = 0.64$. Blue dash-dot line, $\phi = 0.31$.

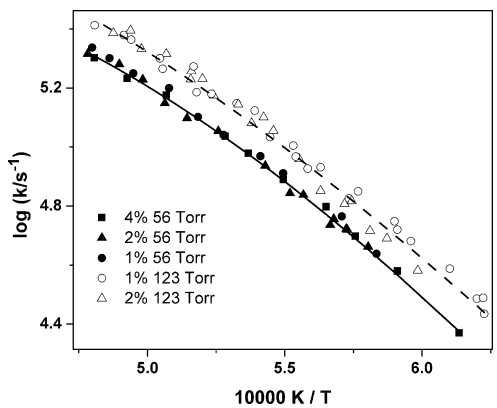


**Fig. 8** Rate coefficients for the initial dissociation of 1,4-dioxane obtained from the laser schlieren experiments with different concentrations' of 1,4-dioxane dilute in krypton. Symbols represent the experimental points and the lines are Arrhenius fits. $P_2 \sim 56$ Torr: ■ 4%$C_4H_8O_2$/Kr; ▲ 2% $C_4H_8O_2$/Kr; ● 1% $C_4H_8O_2$/Kr. $P_2 \sim 123$ Torr: △ 2% $C_4H_8O_2$/Kr; ○ 1% $C_4H_8O_2$/Kr.

reactive flows behind shock waves similar to that outlined in ref. 49 which also accounts for temperature changes due to reaction through solution of the energy equation. Reverse reactions are included for all reactions in the mechanism *via* detailed balance using thermodynamic data taken from the publication of Burcat and Ruscic.[50] Example simulation results are shown in Fig. 2 and similar agreement between simulation and experiment was found over the whole range of the experiments.

The mechanism in Table 2 divides naturally into two parts: Reactions $R_{57}$-$R_{83}$ (the notation $R_x$ refers to a reaction number in Table 2) comprise a sub-mechanism for the reactions of methyl radicals and were taken from recent LS studies on the dissociation of methyl iodide, and of diacetyl,[48,51] that cover a similar range of temperature and pressure. The remaining reactions are associated with the dissociation of 1,4-dioxane, radical attack on the parent and product species, and the dissociation of product species.

A large number of simulations have been performed to test various hypotheses regarding the overall reaction. Again the simulations presented here are based on a mechanism that incorporates dissociation *via* both reactions (1) and (2) for 1,4-dioxane with a slight advantage in rate to dissociation through reaction (2), as suggested by both theory and the TOF-MS results. In the mechanism presented in Table 2 it is assumed that both EGVE and 2EOA dissociate immediately with EGVE forming vinoxy and 2-hydroxyethyl radicals while 2EOA gives vinoxy and ethoxy radicals, in accord with the absence of any sign of early acceleration. Thus reactions $R_1$ and $R_2$ are composites of reaction (1) and (6) and reactions (2) and (8) from the theory section, respectively. Simulations with this model give very good predictions of the experimental density gradients, as seen in Fig. 2. Additional experimental studies are being conducted to study the dissociation of EGVE directly by LS to further address the assumption of rapid decomposition of EGVE and 2EOA. However, again there is no experimental evidence of such a two-step process in 1,4-dioxane analogous to that evident in cyclohexane.[7]

The radical products now undergo further dissociation. Vinoxy by C–C scission with a simultaneous H-atom transfer $R_6$, and elimination of the aldehydic hydrogen, $R_7$. There are several dissociation channels potentially available for dissociation of 2-hydroxyethyl, however at the conditions of the current study elimination of OH by the reverse of reaction $R_3$ is favored. Similar to vinoxy, the ethoxy radical can also dissociate by both C–C scission, $R_4$, and hydrogen elimination, $R_5$.

These processes now generate the required radicals H, OH and $CH_3$ that produce the observed negative gradients and start the chain by abstracting an H-atom from 1,4-dioxane in reactions $R_{12}$, $R_{13}$ and $R_{43}$ respectively. This abstraction forms the 1,4-dioxan-2-yl, whose decomposition ultimately propagates the chain. Here, reaction $R_{13}$, OH + 1,4-dioxane ($\Delta H_{r,298} \sim -22$ kcal/mol), has been studied by Moriarty *et al.*,[52] Maurer *et al.*[53] and Porter *et al.*[54] at 298 K. Their results are in good mutual agreement and provided an initial estimate for $k_{R13}$.

The rate coefficient for reaction $R_{12}$, H + $C_4H_8O_2$, was initially estimated from group parameters,[55] and that of $R_{43}$, $CH_3$ + $C_4H_8O_2$, derived by analogy with $CH_3$ + oxirane.[56] These initial estimates were subsequently refined during the modeling work to the values presented in Table 2. Reaction $R_{43}$ is only mildly exothermic, $\Delta H_{r,298} \sim 9$ kcal/mol, and is relatively slow from both a small rate coefficient and

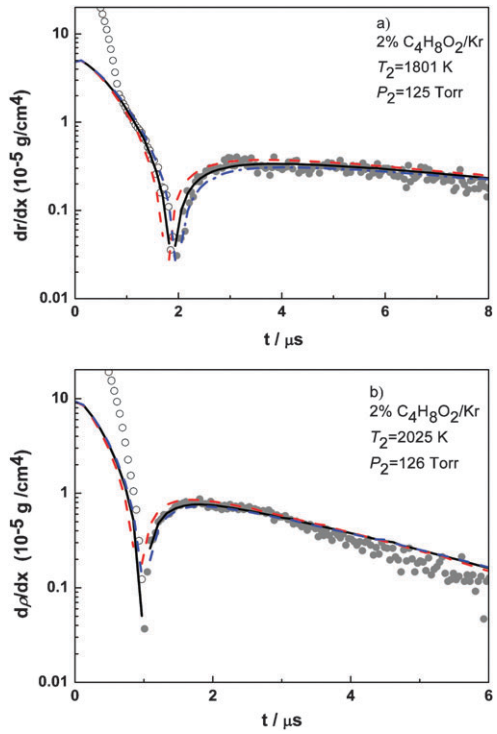


**Fig. 9** Sensitivity of the modeling results to $k_{R12}$, H + $C_4H_8O_2$ → $H_2$ + $C_4H_7O_2$. Absolute values are plotted. Symbols represent experimental data with open symbols corresponding to positive density gradients and closed symbols to negative ones. Lines are the results of simulations. Solid black line, model in Table 2. Red dashed line, $k_{R12}$ × 2.0. Blue dash-dot line, $k_{R12}$ × 0.5.

competition with $R_{21}$ ($CH_3$ + HCO) which readily consumes methyl radicals. Consequently, $R_{43}$ contributes little to either the observed density gradient or the progress of the chain. Reaction $R_{12}$ is also exothermic by just ~8 kcal/mol, however the simulations display sufficient, albeit modest, sensitivity to its rate, as in Fig. 9, enabling the rate to be optimized for each experiment. The values of $k_{R12}$ that give the best fit to the simulation are around a factor 2–4 lower than group additivity predicts for H-atom attack on four secondary carbons and around a factor of 4–6 lower than the theoretical predictions for $k_{R12}$. However, the experiments do not support a higher value, particularly at low temperatures; note Fig. 9.

Similarly, the simulations are quite sensitive to $R_{13}$, OH + 1,4-dioxane, and its rate was also adjusted for each experiment. The bimolecular rate coefficients determined for $R_{12}$ and $R_{13}$ were fitted to non-Arrhenius expressions, given in Table 2, valid over the range 1500–2100 K. The value of $k_{R13}$ is in reasonable agreement with the low temperature determination by Moriarty *et al.*, and is within a factor of two of our own variational transition state theory calculations. With the mechanism in Table 2 the primary sources of negative density gradients at all reaction temperatures are reactions $R_{16}$, H + HCO; $R_{21}$, $CH_3$ + HCO; $R_{26}$, OH + HCO; all of which are roughly 90 kcal/mol exothermic.

The self reaction of methyl radicals makes almost no contribution to the calculated density gradient as the methyl radicals are primarily consumed by reaction $R_{21}$. With the exception of $R_{14}$ the remaining reactions in Table 2 make little contribution to the net density gradient due to low heats of reaction and/or low rates. For a number of unimportant reactions it has been necessary to estimate rate coefficients and these are noted in Table 2, the remaining rate coefficients were obtained from a thorough review of the literature.

The chain reaction in this dissociation is propagated by the formation of the 1,4-dioxan-2-yl and the subsequent decomposition of this radical *via* reactions $R_{14}$(a and b). Here the products are exactly those identified by Lin *et al.*[16] as

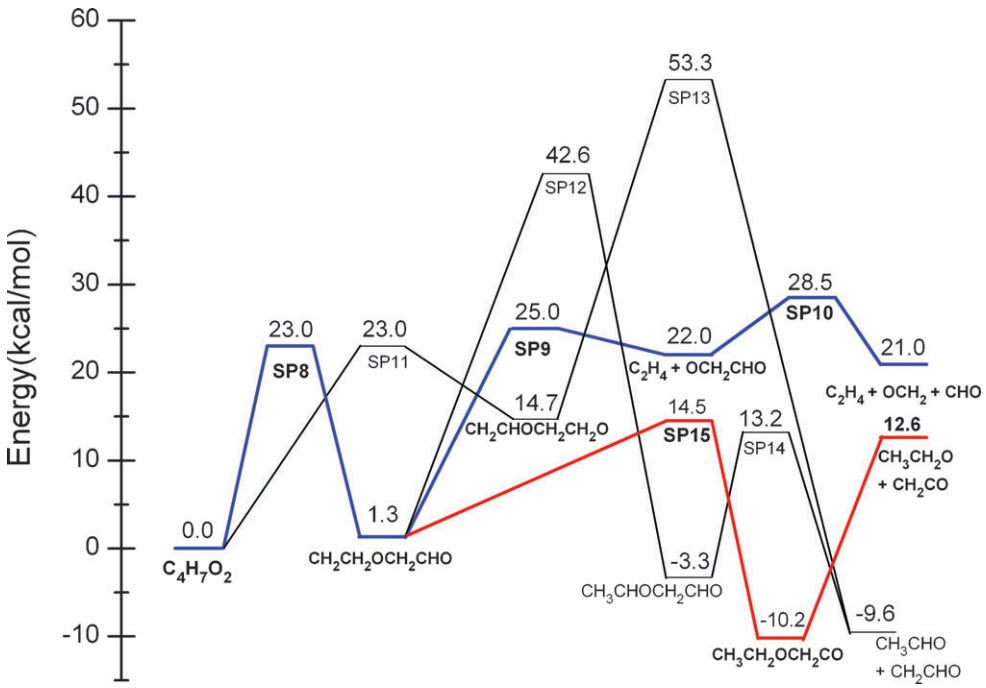


**Fig. 10** G3B3 potential energy surface for the dissociation of $C_4H_7O_2$.

 

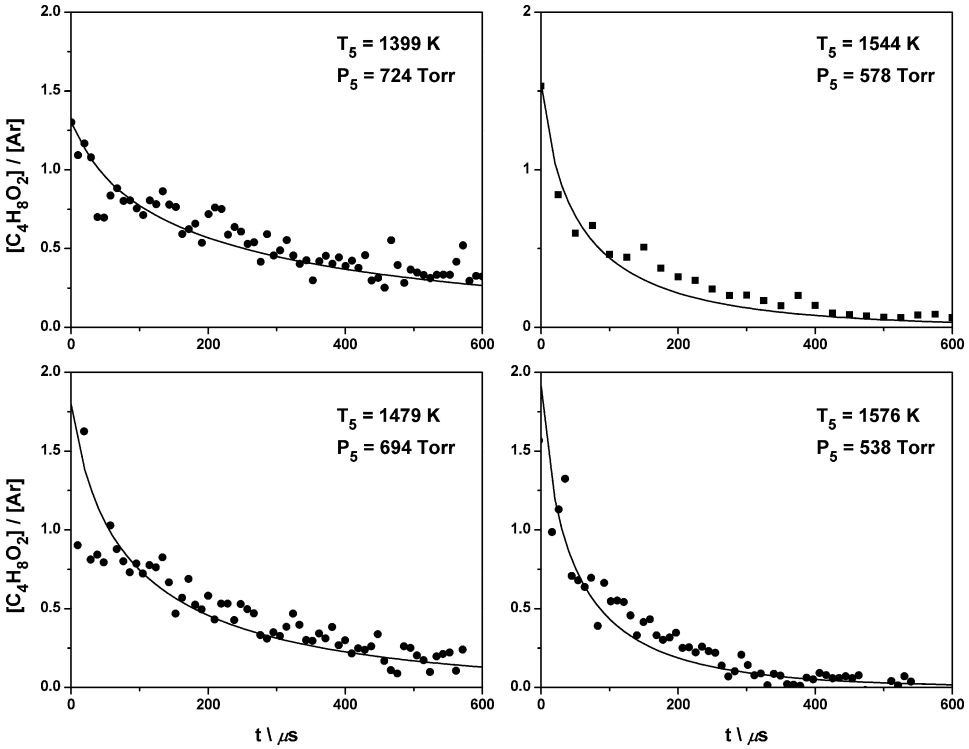


**Fig. 11** Comparison of simulations using the mechanism in Table 2 and TOF-MS results for reagent mixtures containing 4% 1,4-dioxane with 4% argon as an internal standard. All experiments were performed with a repetition rate of 105 kHz with the exception of the upper right panel where the repetition rate was 49kHz.

initial products of $C_4H_7O_2$ dissociation: $C_2H_4$, $CH_2O$, HCO and ethoxy, $CH_3CH_2O$. The decomposition pathways used herein to predict the products of dissociation and to provide an estimate of the activation barrier are actually independent of the Lin *et al*. results, being based on *ab initio* calculations using the G3B3 method. The derived potential energy surface is shown in Fig. 10. Here the cyclic radical can initially dissociate *via* scission of the CO bond adjacent to the radical site with simultaneous H-atom transfer through either SP8 or SP11. Both SP8 and SP11 have very similar energies relative to $C_4H_7O_2$, however, the intermediate formed *via* SP11 has a very high barrier to further reaction. Thus it is most likely that dissociation of $C_4H_7O_2$ will occur predominantly *via* SP8 to generate $CH_2CH_2OCH_2CHO$ which can subsequently dissociate by two paths that differ only by 10–13 kcal. The higher energy path, $R_{14a}$, generates $C_2H_4$, $H_2CO$ and HCO. The subsequent fast decomposition of HCO to H + CO[57] then propagates the chain reaction. The lower energy path, $R_{14b}$, gives ethoxy radicals and ketene. The ethoxy radicals react further through $R_4$ to give methyl radicals and formaldehyde again leading to chain propagation.

The full chain mechanism of 1,4-dioxane decomposition is very complex with many reactions whose rates are unknown, and its modeling is fraught with difficulty. In particular the complex set of reactions involved in the decomposition of the vinoxy radical, here generated in both dissociation steps, and involving its dissociation and H-atom addition and abstraction reactions, presents insurmountable problems with the H-atom balance. The mechanism 'works' in that it produces the entire gradient profile, but rates of all but the two dissociation reactions should be considered in doubt.

Finally, concentration/time profiles of $m/z$ 88, the parent ion of 1,4-dioxane, have been extracted from the TOF-MS experiments and compared with the results of simulations with the model discussed above. In all cases argon is used as an internal standard to account for pressure changes in the ion source[23] and the results are presented as the ratio of the $m/z$ 88 and argon peak areas. Representative results are presented in Fig. 11 and the comparison is quite good. However, it should be noted that the location of $t_0$ has to be estimated in the experimental data and the initial point of the simulation is scaled to match the pre-shock portion of the experimental results.

## Conclusion

A detailed investigation of the pyrolysis of 1,4-dioxane using complementary experimental and theoretical methods has demonstrated that the dissociation does not occur *via* concerted molecular reaction like that in trioxane,[1–5] but rather by ring opening, isomerization, and dissociation of the resulting linear species to generate H, OH and $CH_3$ radicals that propagate an exothermic chain mechanism. The initial modeling results indicate that the LS profiles can be satisfactorily simulated with the mechanism in Table 2 that assumes dissociation/isomerization of 1,4-dioxane forming both of the linear molecules $HOCH_2CH_2OCHCH_2$ (EGVE) and $CH_3CH_2OCH_2CHO$ (2EOA), which then themselves rapidly dissociate by central fission ultimately forming the cited radicals. This dissociation mechanism is completely different than anything in the literature and represents the

results of the first serious look at this process in a cyclic ether with fewer than three O-atoms.

## Acknowledgements

Helpful discussions with Lawrence B. Harding and James A. Miller are gratefully acknowledged. This work was performed under the auspices of the Office of Basic Energy Sciences, Division of Chemical Sciences, Geosciences, and Biosciences, U.S. Department of Energy, under contract numbers DE-AC02-06CH11357, DE-AC04-94-AL85000, DE-FE-85ER13384.

## References

1 V. Vasudevan, D. F. Davidson, R. K. Hanson, C. T. Bowman and D. M. Golden, *Proc. Combust. Inst.*, 2007, **31**, 175–183.
2 S. Hochgreb and F. L. Dryer, *J. Phys. Chem.*, 1992, **96**, 295–297.
3 H. K. Aldridge, X. Liu, M. C. Lin and C. F. Melius, *Int. J. Chem. Kinet.*, 1991, **23**, 947–956.
4 E. A. Irdam and J. H. Kiefer, *Chem. Phys. Lett.*, 1990, **166**, 491–494.
5 W. Hogg, D. M. McKinnon, A. J. Trotman-Dickenson and G. J. O Verbeke, *J. Chem. Soc.*, 1961, 1403–1404.
6 W. Tsang, *Int. J. Chem. Kinet.*, 1978, **10**, 1119–1138.
7 J. H. Kiefer, K. S. Gupte, L. B. Harding and S. J. Klippenstein, *J. Phys. Chem. A*, 2009, **113**, 13570–13583.
8 L. Kuchler and J. D. Lambert, *Zeit. Physik. Chem.*, 1936, **37B**, 285.
9 F. Battin, P. M. Marquaire, F. Baronnet and G. M. Come, *J. Anal. Appl. Pyrolysis*, 1989, **16**, 345–354.
10 E. A. Irdam, J. H. Kiefer, L. B. Harding and A. F. Wagner, *Int. J. Chem. Kinet.*, 1993, **25**, 285–303.
11 S. S. Kumaran, J. J. Carroll and J. V. Michael, *Symp. (Int.) Combust., Proc.*, 1998, **27**, 125–133.
12 J. H. Kiefer, S. A. Kapsalis, M. Z. Alalami and K. A. Budach, *Combust. Flame*, 1983, **51**, 79–93.
13 T. Tanzawa and W. C. Gardiner, *Combust. Flame*, 1980, **39**, 241–253.
14 T. Just, P. Roth and R. Damm, *Symp. (Int.) Combust., [Proc.]*, 1977, **16**, 961–969.
15 D. L. Baulch, C. T. Bowman, C. J. Cobos, R. A. Cox, T. Just, J. A. Kerr, M. J. Pilling, D. Stocker, J. Troe, W. Tsang, R. W Walker and J. Warnatz, *J. Phys. Chem. Ref. Data*, 2005, **34**, 757–1397.
16 Z. Lin, D. Han, S. Li, Y. Li and T. Yuan, *J. Phys. Chem. A*, 2009, **113**, 1800–1806.
17 B. Sirjean, P. A. Glaude, M. F. Ruiz-Lopez and R. Fournet, *J. Phys. Chem. A*, 2006, **110**, 12693–12704.
18 R. S. Tranter, X. Yang, *unpublished.*
19 R. S. Tranter and B. R. Giri, *Rev. Sci. Instrum.*, 2008, **79**, 094103.
20 J. H. Kiefer, in *Shock Waves in Chemistry*, ed. A. Lifshitz, Marcel Dekker, New York, 1981, ch. 5, pp. 219–277.
21 J. H. Kiefer and A. C. Manson, *Rev. Sci. Instrum.*, 1981, **52**, 1392–1396.
22 W. C. Gardiner, Y. Hidaka and T. Tanzawa, *Combust. Flame*, 1981, **40**, 213–219.
23 R. S. Tranter, B. R. Giri and J. H. Kiefer, *Rev. Sci. Instrum.*, 2007, **78**, 034101.
24 S. E. Stein, Mass Spectra, *NIST Chemistry WebBook, NIST Standard Reference Database Number 69*, 2010.
25 J. A. Pople, M. Head-Gordon and K. Raghavachari, *J. Chem. Phys.*, 1987, **87**, 5968–5975; K. Raghavachari, G. W. Trucks, J. A. Pople and M. Head-Gordon, *Chem. Phys. Lett.*, 1989, **157**, 479–483.
26 A. D. Becke, *J. Chem. Phys.*, 1993, **98**, 5648–5652; C. Lee, W. Yang and R. G. Parr, *Phys. Rev. B*, 1988, **37**, 785.
27 R. Krishnan, J. S. Binkley, R. Seeger and J. A. Pople, *J. Chem. Phys.*, 1980, **72**, 650–654; T. Clark, J. Chadrasekhar and P. v. R. Schleyer, *J. Comput. Chem.*, 1983, **4**, 294–301.
28 J. M. L. Martin and O. Uzan, *Chem. Phys. Lett.*, 1998, **282**, 16–24.
29 T. H. Dunning Jr., *J. Chem. Phys.*, 1989, **90**, 1007–1023.
30 T. J. Lee, A. P. Rendell and P. R. Taylor, *J. Phys. Chem.*, 1990, **94**, 5463–5468.
31 K. Andersson, P. A. Malmqvist and B. O. Roos, *J. Chem. Phys.*, 1992, **96**, 1218–1226; H.-J. Werner, *Mol. Phys.*, 1996, **89**, 645–661; P. Celani and H.-J. Werner, *J. Chem. Phys.*, 2000, **112**, 5546–5557; P. Celani and H.-J. Werner, *J. Chem. Phys.*, 2003, **119**, 5044–5057.
32 R. A. Kendall, T. H. Dunning Jr. and R. J. Harrison, *J. Chem. Phys.*, 1992, **96**, 6796–6806.
33 S. R. Langhoff and E. R. Davidson, *Int. J. Quantum Chem.*, 1974, **8**, 61–72; D. W. Silver and E. R. Davidson, *Chem. Phys. Lett.*, 1978, **52**, 403–406.
34 H.-J. Werner and P. J. Knowles, *J. Chem. Phys.*, 1988, **89**, 5803–5814; P. J. Knowles and H.-J. Werner, *Chem. Phys. Lett.*, 1988, **145**, 514–522.
35 A. G. Baboul, L. A. Curtiss, P. C. Redfern and K. Raghavachari, *J. Chem. Phys.*, 1999, **110**, 7650.
36 B. J. Lynch, P. L. Fast, M. Harris and D. G. Truhlar, *J. Phys. Chem. A*, 2000, **104**, 4811–4815.
37 D.-H. Lu, T. N. Truong, V. S. Melissas, G. C. Lynch, Y.-P. Liu, B. C. Garrett, R. Steckler, A. D. Isaacson, S. N. Rai, G. Hancock, J. G. Lauderdale, T. Joseph and D. G. Truhlar, *Comput. Phys. Commun.*, 1992, **71**, 235–262; Y.-P. Liu, G. C. Lynch, T. N. Truong, D.-H. Lu and D. G. Truhlar, *J. Am. Chem. Soc.*, 1993, **115**, 2408–2415.
38 M. J. Frisch, G. W. Trucks, H. B. Schlegel, G. E. Scuseria, M. A. Robb, J. R. Cheeseman, J. A. Montgomery Jr., T. Vreven, K. N. Kudin, J. C. Burant, J. M. Millam, S. S. Iyengar, J. Tomasi, V. Barone, B. Mennucci, M. Cossi, G. Scalmani, N. Rega, G. A. Petersson, H. Nakatsuji, M. Hada, M. Ehara, K. Toyota, R. Fukuda, J. Hasegawa, M. Ishida, T. Nakajima, Y. Honda, O. Kitao, H. Nakai, M. Klene, X. Li, J. E. Knox, H. P. Hratchian, J. B. Cross, V. Bakken, C. Adamo, J. Jaramillo, R. Gomperts, R. E. Stratmann, O. Yazyev, A. J. Austin, R. Cammi, C. Pomelli, J. W. Ochterski, P. Y. Ayala, K. Morokuma, G. A. Voth, P. Salvador, J. J. Dannenberg, V. G. Zakrzewski, S. Dapprich, A. D. Daniels, M. C. Strain, O. Farkas, D. K. Malick, A. D. Rabuck, K. Raghavachari, J. B. Foresman, J. V. Ortiz, Q. Cui, A. G. Baboul, S. Clifford, J. Cioslowski, B. B. Stefanov, G. Liu, A. Liashenko, P. Piskorz, I. Komaromi, R. L. Martin, D. J. Fox, T. Keith, M. A. Al-Laham, C. Y. Peng, A. Nanayakkara, M. Challacombe, P. M. W. Gill, B. Johnson, W. Chen, M. W. Wong, C. Gonzalez and J. A. Pople, *Gaussian 03, Revision C.02*, Gaussian, Inc., Wallingford CT, 2004.
39 H.-J. Werner, P. J. Knowles, R. Lindh, F. R. Manby, M. Schütz, P. Celani, T. Korona, A. Mitrushenkov, G. Rauhut, T. B. Adler, R. D. Amos, A. Bernhardsson, A. Berning, D. L. Cooper, M. J. O. Deegan, A. J. Dobbyn, F. Eckert, E. Goll, C. Hampel, G. Hetzer, G. Knizia, C. Köppl, Y. Liu, A. W. Lloyd, R. A. Mata, A. J. May, S. J. McNicholas, W. Meyer, M. E. Mura, A. Nicklaß, P. Palmieri, K. Pflüger, R. Pitzer, M. Reiher, U. Schumann, H. Stoll, A. J. Stone, R. Tarroni, T. Thorsteinsson, M. Wang and A. Wolf, *MOLPRO, Version*, 2009.
40 W. Duch and G. H. F. Diercksen, *J. Chem. Phys.*, 1994, **101**, 3018–3030.
41 L. B. Harding, S. J. Klippenstein and A. W. Jasper, *Phys. Chem. Chem. Phys.*, 2007, **9**, 4055–4070.
42 F. Freeman and K. Uyen Do, *THEOCHEM*, 2002, **577**, 43–54.
43 D. A. Dixon and A. Komornicki, *J. Phys. Chem.*, 1990, **94**, 5630–5636.
44 J. P. Senosiain, S. J. Klippenstein and J. A. Miller, *J. Phys. Chem. A*, 2006, **110**, 5772–5781.
45 Z. F. Xu, K. Xu and M. C. Lin, *ChemPhysChem*, 2009, **10**, 972–982.
46 J. H. Kiefer, M. Z. Alalami and J. C. Hajduk, *Appl. Opt.*, 1981, **20**, 221–230.
47 J. H. Kiefer, S. S. Kumaran and S. Sundaram, *J. Chem. Phys.*, 1993, **99**, 3531–3541.
48 X. Yang, C. F. Goldsmith and R. S. Tranter, *J. Phys. Chem. A*, 2009, **113**, 8307–8317.
49 W. C. Gardiner, B. F. Walker and C. B. Wakefield, in *Shock Waves in Chemistry*, ed. A. Lifshitz, Marcel Dekker inc, New York, 1981, ch. 7, pp. 319–374.
50 A. Burcat and B. Ruscic, *Ideal Gas Thermochemical Database with updates from Active Thermochemical Tables*, ⟨*ftp://ftp.technion.ac.il/pub/supported/aetdd/thermodynamics*⟩ March 2010.

 

51 X. Yang, A. W. Jasper, J. H. Kiefer and R. S. Tranter, *J. Phys. Chem. A*, 2009, **113**, 8318–8326.
52 J. Moriarty, H. Sidebottom, J. Wenger, A. Mellouki and G. Le Bras, *J. Phys. Chem. A*, 2003, **107**, 1499–1505.
53 T. Maurer, H. Hass, I. Barnes and K. H. Becker, *J. Phys. Chem. A*, 1999, **103**, 5032–5039.
54 E. Porter, J. Wenger, J. Treacy, H. Sidebottom, A. Mellouki, S. Teton and G. LeBras, *J. Phys. Chem. A*, 1997, **101**, 5770–5775.
55 T. Ogura, A. Miyoshi and M. Koshi, *Phys. Chem. Chem. Phys.*, 2007, **9**, 5133–5142.
56 R. R. Baldwin, A. Keen and R. W. Walker, *J. Chem. Soc., Faraday Trans. 1*, 1984, **80**, 435–456.
57 G. Friedrichs, J. T. Herbon, D. F. Davidson and R. K. Hanson, *Phys. Chem. Chem. Phys.*, 2002, **4**, 5778–5788.
58 J. P. Senosiain, S. J. Klippenstein and J. A. Miller, *J. Phys. Chem. A*, 2006, **110**, 6960–6970.
59 M. H. Matus, M. T. Nguyen and D. A. Dixon, *J. Phys. Chem. A*, 2007, **111**, 113–126.
60 G. P. Smith, D. M. Golden, M. Frenklach, N. W. Moriarty, B. Eiteneer, M. Goldenberg, C. T. Bowman, R. K. Hanson, S. Song, W. C. Gardiner, V. V. Lissianski and Z. Qin, GRIMech 3.0. http://www.me.berkeley.edu/gri_mech/.
61 J. Troe, *J. Phys. Chem. A*, 2007, **111**, 3862–3867.
62 H. Hou, B. S. Wang and Y. S. Gu, *Phys. Chem. Chem. Phys.*, 2000, **2**, 2329–2334.
63 V. Vasudevan, D. F. Davidson and R. K. Hanson, *Int. J. Chem. Kinet.*, 2005, **37**, 98–109.
64 M. S. Wooldridge, R. K. Hanson and C. T. Bowman, *Int. J. Chem. Kinet.*, 1996, **28**, 361–372.
65 N. K. Srinivasan, M. C. Su, J. W. Sutherland and J. V. Michael, *J. Phys. Chem. A*, 2005, **109**, 1857–1863.
66 A. W. Jasper, S. J. Klippenstein, L. B. Harding and B. Ruscic, *J. Phys. Chem. A*, 2007, **111**, 3932–3950.
67 N. K. Srinivasan, M. C. Su and J. V. Michael, *J. Phys. Chem. A*, 2007, **111**, 3951–3958.
68 S. R. Sellevag, Y. Georgievskii and J. A. Miller, *J. Phys. Chem. A*, 2008, **112**, 5085–5095.
69 J. P. Senosiain, S. J. Klippenstein and J. A. Miller, *J. Phys. Chem. A*, 2005, **109**, 6045–6055.
70 L. N. Krasnoperov and J. V. Michael, *J. Phys. Chem. A*, 2004, **108**, 5643–5648.
71 R. Sivaramakrishnan, J. V. Michael and S. J. Klippenstein, *J. Phys. Chem. A*, 2010, **114**, 755–764.
72 P. Frank, K. A. Bhaskaran and T. Just, *J. Phys. Chem.*, 1986, **90**, 2226–2231.
73 W. Tsang, *J. Phys. Chem. Ref. Data*, 1987, **16**, 471–508.